Chemistry Europe
European Chemical Societies Publishing

WILEY VCH

Excellence in Chemistry Research

Announcing our new flagship journal

- Gold Open Access
- Publishing charges waived
- Preprints welcome
- Edited by active scientists

Meet the Editors of *ChemistryEurope*

Luisa De Cola
Università degli Studi di Milano Statale, Italy

Ive Hermans
University of Wisconsin-Madison, USA

Ken Tanaka
Tokyo Institute of Technology, Japan

Chemistry–A European Journal
Research Article
doi.org/10.1002/chem.202300996
Chemistry Europe
European Chemical Societies Publishing
www.chemeurj.org

Special Collection

N-Alkylated Pyridoxal Derivatives as Negative Electrolyte Materials for Aqueous Organic Flow Batteries: Computational Screening**

Andrea Hamza,*[a] Flóra B. Németh,[a] Ádám Madarász,[a] Anton Nechaev,[b] Petri M. Pihko,[b] Pekka Peljo,[c, d] and Imre Pápai*[a]

Abstract: N-functionalized pyridinium frameworks derived from the three major vitamers of vitamin B6, pyridoxal, pyridoxamine and pyridoxine, have been screened computationally for consideration as negative electrode materials in aqueous organic flow batteries. A molecular database including the structure and the one-electron standard reduction potential of related pyridinium derivatives has been generated using a computational protocol that combines semi-empirical and DFT quantum chemical methods. The predicted reduction potentials span a broad range for the investigated pyridinium frameworks, but pyridoxal derivatives, particularly those involving electron withdrawing substituents, have potentials compatible with the electrochemical stability window of aqueous electrolytes. The stability of radicals formed upon one-electron reduction has been analyzed by a new computational tool proposed recently for large-scale computational screening.

Introduction

Replacement of fossil fuels with renewable energy sources is critical for reducing the CO_2 emissions. Consequently, intermittent energy sources, such as wind and solar power, need to be integrated into the electrical grid in an enormously large scale, and they should also be coupled with energy storage. To some extent, pumped hydro power is already used for this purpose, but additional immense energy storage capacities are urgently required, as the share of the intermittent energy sources is gradually increasing.[1] Batteries are an obvious choice for this purpose, but the conventional solid-state batteries are too expensive for large scale deployment in the TWh energy range because they require critical and scarce resources, such as Li, Co, Ni, or V, and their cycle life is relatively short.[2] Flow batteries (FBs) represent a viable solution to grid-scale renewable energy storage, as the storage capacity and the power can be easily scaled by increasing the size of the electrolyte tanks, and by the number of cell stacks.[3] Vanadium-based flow batteries are the most developed technologies available commercially[4] but their large-scale deployment is limited due to the high cost of the raw materials. Therefore, alternative options utilizing abundant materials for large-scale energy storage are highly needed.

Recently, there has been growing effort to develop flow batteries using organic redox molecules as electrolyte materials.[5] The main advantage of this approach is that the crucial physico-chemical properties of potential candidate compounds that influence the performance of FBs can be tailored by functionalization of a diverse set of molecular frameworks. Currently, the development of aqueous organic redox couples is in major focus in FB research,[6] but non-aqueous FBs are considered as possible alternatives as well.[7] The design criteria for organic redox molecules are quite restrictive. In addition to high energy and power density, suitable redox potential, and stability over thousands of cycles, the molecules will also need to be highly soluble, safe, and easily accessible in large scale. As the traditional trial-and-error based approach for development of new redox couples is very time consuming and expensive even with the most advanced

[a] Dr. A. Hamza, F. B. Németh, Dr. Á. Madarász, Prof. I. Pápai
Institute of Organic Chemistry
Research Centre of Natural Sciences
Magyar tudósok körutja 2, 1117 Budapest (Hungary)
E-mail: papai.imre@ttk.hu
hamza.andrea@ttk.hu
[b] Dr. A. Nechaev, Prof. P. M. Pihko
Department of Chemistry
University of Jyväskylä
P. O. Box 35, 40014, Jyväskylä (Finland)
[c] Dr. P. Peljo
Research Group of Battery Materials and Technologies
Department of Mechanical and Materials Engineering
Faculty of Technology, University of Turku
20014 Turku (Finland)
[d] Dr. P. Peljo
Department of Chemistry and Materials Science
Aalto University
FI-00076 Aalto (Finland)

[**] A previous version of this manuscript has been deposited on a preprint server (https://doi.org/10.26434/chemrxiv-2023-bzc6w).

Supporting information for this article is available on the WWW under https://doi.org/10.1002/chem.202300996

Special Collection Part of the Special Collection "Battery Research in Europe".

experimental screening techniques, several studies have aimed to accelerate this process by computational screening studies.[8] The effect of various substituents on the reduction potential and the solubility of quinone derivatives[9] and phenazines[10] have been explored computationally, and the trends revealed by structure-property analysis could serve as useful guidance for tuning these properties. Combinatorial generation of extended molecular databases via quantum chemical calculations followed by virtual screening[11] has proven to be an efficient approach to identify promising candidates for experimental validation.[12] The application of machine learning techniques as high-throughput screening tools can particularly advance the discovery of new electrolyte materials.[13]

Computational screening studies have mostly focused on compounds undergoing $2e^-/2H^+$ proton coupled electron transfer redox processes, but molecular frameworks that do not involve protonation processes in their redox equilibria are also of significant interest. N-alkylated bipyridinium derivatives, such as viologens, for instance, have been demonstrated as promising aqueous negative electrolytes in pH neutral conditions.[14] Benzoylpyridinium compounds have also been proposed as organic electrolytes for both aqueous and non-aqueous FBs.[15] *N*-functionalized pyridinium species can readily undergo $1e^-$ or $2e^-$ reduction processes with desirable reduction potentials, however, stability issues are often encountered due to the reactivity of radical species formed upon the first reduction event, which confines their practical application. Large-scale computational screening for this family of redox active compounds could be beneficial in that respect.

In our present work, we consider *N*-functionalized pyridinium frameworks derived from various B6 vitamers (pyridoxal, pyridoxamine and pyridoxine; see Scheme 1) as potential candidates for aqueous negative electrolytes, and we assess their relevance via computational screening. In principle, these quaternary pyridinium salts can be synthesized by N-alkylation[16] and additional targeted functionalizations of the parent pyridines, which are natural products and commercially available as phosphorylated variants. The choice of the B6 nucleus was based on two potential benefits: first, the vitamers might be available via fermentation in sufficiently large scale for eventual FB purposes, and second, the pyridoxal/pyridoxine core is already densely functionalized with potential hydrophilic groups that could increase solubility in water. To assist in the choice of synthetic candidates, herein we present an automated computational protocol that enables to build a large-scale molecular library of molecular structures and accurate $1e^-$ standard reduction potentials. This protocol is applied to B6 vitamin derivatives and we expect that the analysis of the developed molecular database allows us to identify a class of pyridinium derivatives with reduction potentials compatible with the electrochemical stability of aqueous electrolytes. The stabilities of reduced states of pyridinium derivatives are assessed in terms of radical stability descriptors suggested recently by St. John and Paton.[17]

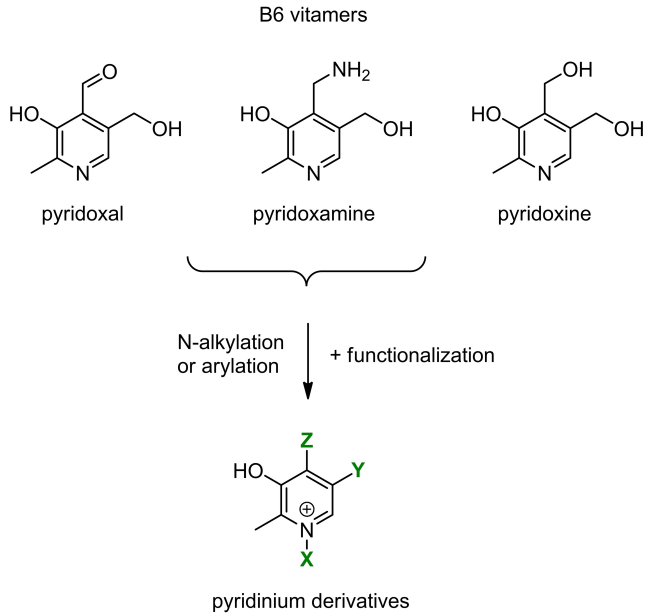

Scheme 1. Synthetic strategy towards pyridinium derivatives.

Pyridinium frameworks

Five different molecular sets, denoted as pyr1, pyr2, …, pyr5, were chosen to generate the present database, which will be referred to as B6-PYR (Scheme 2). Label "PYR" refers to the pyridinium unit, which is a common feature of N-alkylated/arylated B6 vitamer derivatives. The pyr1 set involves over 3000 molecules derived by the combination of three substituents R_1, R_2 and R_3 on the pyridinium core. Substituent R_1 is an N-alkyl or an N-aryl group with varying size and electron donor property (P1 to P8 in Scheme 2). The steric properties of the nitrogen substituent were found to correlate with the persistence of benzoylpyridinium radicals.[15d] R_2 represents a large set of substituents at the *meta* position of the pyridinium ring with a broad range of electron withdrawing and donating functionalities as well as charged units that could potentially increase aqueous solubility (e.g. phosphate, sulphate, quaternary ammonium groups). We are aware that some of these substituent patterns could be challenging to access from the pyridoxine/pyridoxal core or otherwise, but we nevertheless opted to deploy a large variety of substituents in the study to explore their influence on the standard reduction potential. Substituent R_3 is typically a carboxyl or a keto group in the *para* position (A, B and C in Scheme 2), so these molecules can be considered as pyridoxal derivatives, but in some cases R_3 is a hydroxymethyl group (F). Molecular sets pyr2 and pyr3 are basically pyridoxamine derivatives, where R_3 is either an isopropyl or a phenyl group (D and E). Two additional fused ring structures, cyclic phosphate (pyr4) and cyclic acetal (pyr5) sets, derived from pyridoxine were also introduced with varying R_1 and R_2 groups (Scheme 2). All considered combinations of the five pyridinium frameworks and the three substituents result in a set of compounds with a total number of 6712 molecules (for specific combinations, see Table S1 in the Supporting Information).

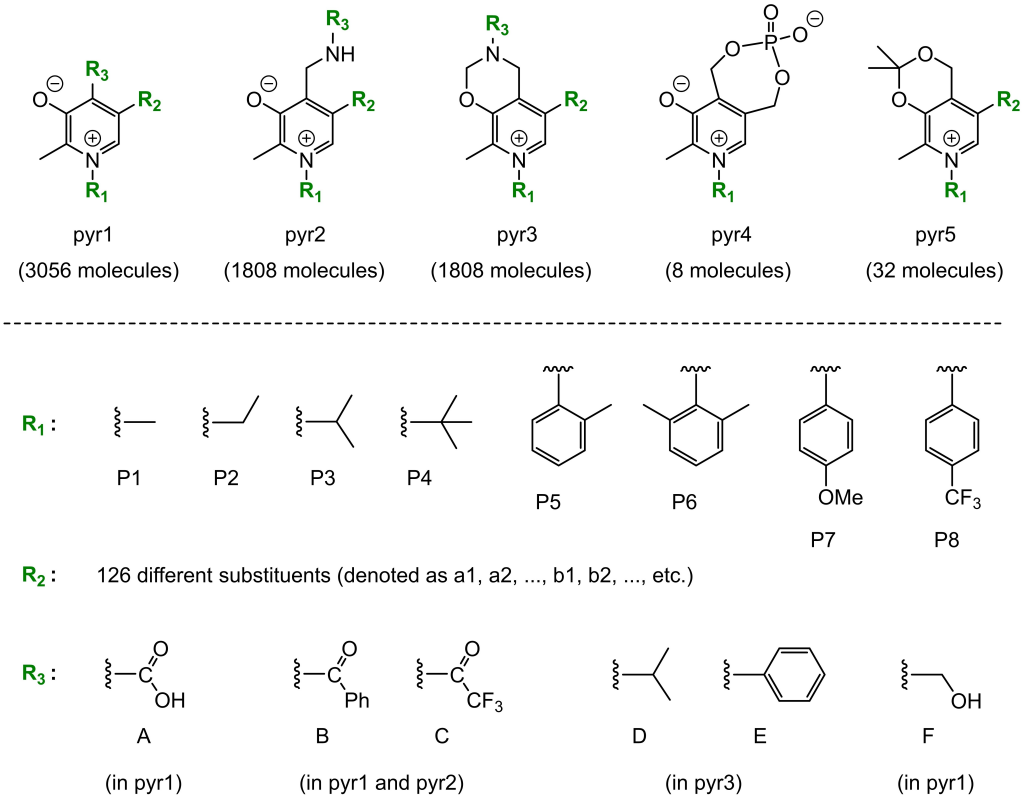

Scheme 2. Pyridinium-based molecular sets derived from B6 vitamer frameworks. More detailed information regarding the particular combination of the substituents and the specification of the R_2 substituents are provided in the Supporting Information.

Computational protocol

Among the key properties of redox active organic compounds, the redox potential can be computed with reasonable accuracy using density functional theory (DFT) calculations.[18] However, accurate predictions of absolute solubilities and computational evaluation of electrochemical or chemical stabilities of redox couples remain a challenge.[19,20] In our present work, the computational screening of pyridinium derivatives is primarily based on $1e^-$ standard reduction potentials, but we address the stability of the reduced species as well. To fulfill the basic requirements of high-throughput computational screening, namely to be able to generate and analyze a large dataset of sufficient accuracy within acceptable timeframe, we established a computational protocol that involves several cheminformatics tools and the application of different levels of quantum chemical methods. In this section, we summarize the basic elements of this protocol (see flowchart in Figure 1).

The 2D structures of pyridinium derivatives were generated in a combinatorial manner from the predefined molecular cores (pyr1-pyr5 frameworks) and a set of substituents (R_1, R_2 and R_3) using the *CombiGlide* and *LigPrep* modules of the Schrödinger package.[21] The protonation state of each molecule was set up by the *Epic* module according to pH = 7 in water. The initial 3D structures of all molecules involved in the database were generated by OpenBabel.[22]

The initial geometries were preoptimized in aqueous phase using the semiempirical extended tight-binding GFN2-xTB method[23] as implemented in the *xtb* program package (version 6.4).[24] The same method was used for conformational search, which was carried out via the *crest* utility of the *xtb* program separately for both oxidized and reduced forms of the molecules. The Conformer-Rotamer Ensemble Sampling Tool (CREST) procedure[25] employs extensive metadynamic sampling and additional genetic Z-matrix crossing algorithms. The relative stabilities of identified conformers were ranked according to the aqueous-phase Gibbs free energies, and for each species, the most favored conformers were selected for redox potential calculations. The solvent effects were incorporated implicitly via the generalized Born-model with surface area contributions (GBSA) as implemented in *xtb*. The rigid-rotor harmonic-oscillator (RRHO) approximation was used to estimate the thermal and entropic contributions to Gibbs free energies at T = 298 K.

The GFN2-xTB optimized structures were used to carry out single-point DFT energy calculations. In DFT calculations we used Truhlar's M06-2X functional[26] along with the 6−311 + G** basis set as implemented in *Gaussian 16*.[27] This basis set was tested against a more extended basis set, and it was found to be sufficient for energy predictions (for details, see the benchmark calculations in the Supporting Information). Solvation effects were estimated via the SMD implicit solvation model.[28]

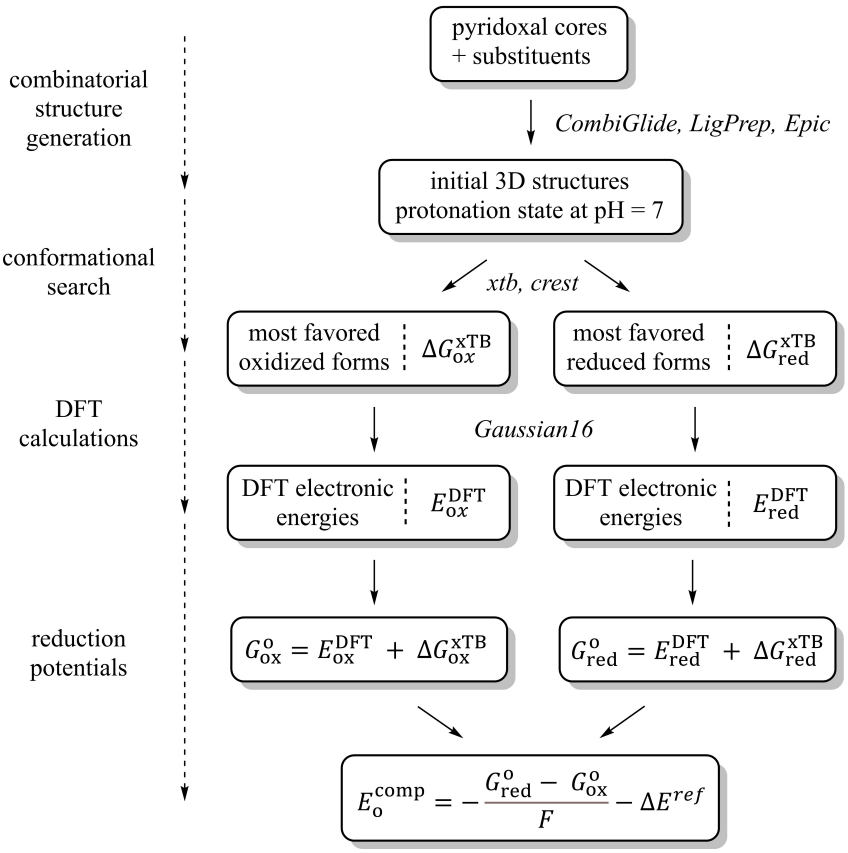

Figure 1. Flowchart of the computational protocol used to generate the pyridinium database.

The standard redox potentials of pyridinium derivatives were computed by the Nernst equation [Equation (1)] as

$$E_{o}^{comp} = -\frac{G_{red}^{o} - G_{ox}^{o}}{F} - \Delta E^{ref} \quad (1)$$

where G_{red}^{o} and G_{ox}^{o} are the aqueous phase Gibbs free energies of the reduced and oxidized forms of pyridinium species, F is the Faraday constant, and ΔE^{ref} is the absolute potential of the reference SHE electrode (4.281 V).[29] The Gibbs free energies were computed via a composite manner [Equation (2)]:

$$G_{ox/red}^{o} = E_{ox/red}^{DFT} + \Delta G_{ox/red}^{xTB} \quad (2)$$

where $E_{ox/red}^{DFT}$ refers to the electronic energy term with the inclusion of solvent effects computed at the DFT level, and $\Delta G_{ox/red}^{xTB}$ involves all finite temperature contributions estimated with the GFN2-xTB method.

The main advantage of using this composite computational protocol, from herein referred to as the GFN2-xTB/M06-2X protocol, is that the computationally most demanding procedures (geometry optimizations, conformational analysis and vibrational analysis) are carried out with the semiempirical GFN2-xTB method, whereas the electronic energies, which represent a critical component of reliable free energy predictions, are computed at a more accurate DFT level. This approach is in line with the concept of high-throughput computational screening, and allows us to build an extended molecular database.

Benchmark studies

To assess the performance of the developed computational protocol, we computed the redox potentials of over 160 organic molecules, for which experimental data are available.[30] The database reported by Nicewicz et al. includes half-peak potentials for a variety of organic compounds, which were obtained via cyclic voltammetry (CV) using the same experimental conditions. The CV measurements were carried out for acetonitrile solutions, and the reported redox potentials were referenced to saturate calomel electrode (SCE), therefore, our computational protocol has been adapted accordingly (for details, see the Supporting Information). The correlation between the calculated and the experimental redox potentials is illustrated in Figure 2.

The linear fitting reveals reasonable correlation with experimental data with $R^2 = 0.95$ and MAE = 0.22 V metrics, although several outlying data points with notable deviations from the linear relationship are seen on the plot (for details, see Figure S1 in the Supporting Information). Redox potentials predicted by the present GFN2-xTB/M06-2X protocol correlate remarkably

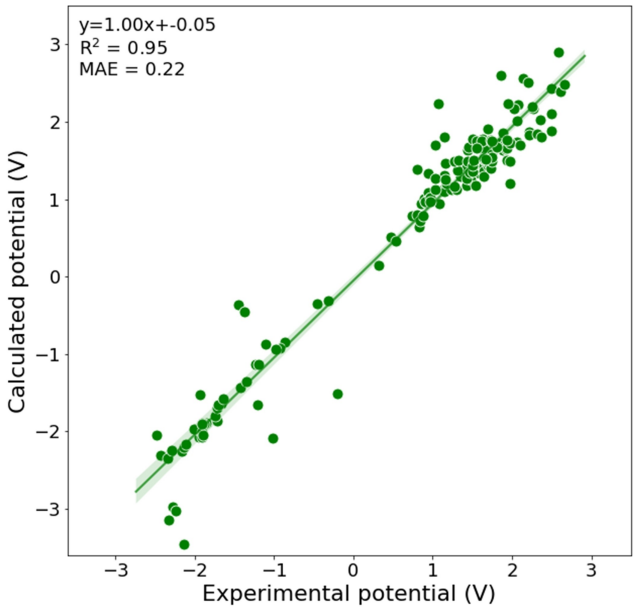

Figure 2. Plot of experimental vs. calculated redox potentials for a set of 162 organic compounds. R^2 and MAE refer to determination coefficient of the least squares linear fitting and mean absolute error with respect to experimental data. The confidence interval for the regression estimate is depicted in light green band.

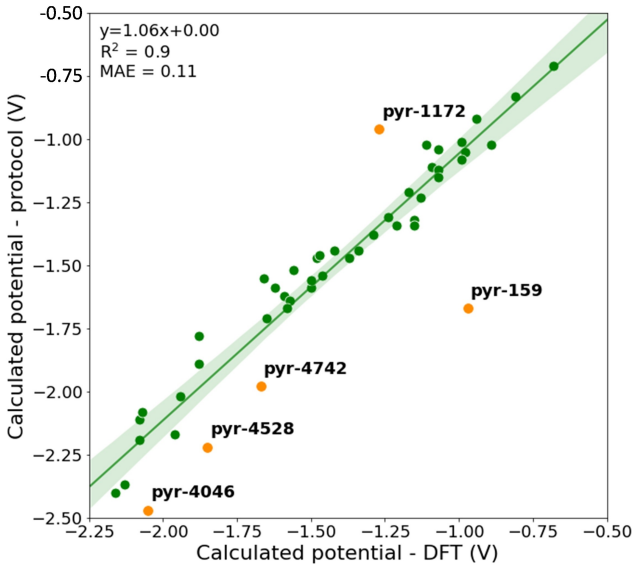

Figure 3. Results of benchmark calculations for a selection of 50 pyridinium molecules. Data points with largest deviations are highlighted in orange.

well with those of full DFT calculations carried out at the M06-2X/6-31 + G(d,p) level by Nicewicz et al. for the same molecular set (see Figure S2 in the Supporting Information), which justifies our composite approach for the estimation of solution-phase Gibbs free energies. We note that the GFN2-xTB/M06-2X protocol seemingly outperforms the full GFN2-xTB method, which yields $R^2 = 0.94$ and MAE = 0.29 V for the same set of organic molecules, and the quality of the GFN2-xTB/M06-2X results is almost identical to high-level full DFT calculations using the double-hybrid PWPB95-D4 functional ($R^2 = 0.93$ and MAE = 0.22 V; see Figures S3 and S4 in the Supporting Information).[18e]

Additional benchmark calculations were carried out for a small subset of pyridinium derivatives (50 molecules). These molecules were selected from the B6-PYR database via a criterion to maximize the structural diversity of the test set, and the main goal was to assess the accuracy of the GFN2-xTB/M06-2X protocol with respect to full DFT calculations for pyridinium derivatives. The most stable forms of these molecules as obtained from the CREST conformational analysis were reoptimized at the M06-2X/6-311G(d,p) level in solution phase (SMD model, water as a solvent), and all thermal and entropic contributions were computed at this level as well. Single-point electronic energy calculations were carried out with the slightly extended 6–311 + G(d,p) basis set used in the GFN2-xTB/M06-2X protocol.

The scatter plot of computed reduction potentials is depicted in Figure 3 and shows a satisfactory linear correlation for the majority of the molecules. Only a few data points deviate significantly from the fitted line. Structural analysis of these molecules revealed marked differences between the structures optimized with the semiempirical GFN2-xTB and the DFT M06-2X methods. For instance, the reduced form of the pyridinium species denoted **pyr-159** displays a ring unit when the geometry optimization is carried out with the GFN2-xTB method, whereas this ring structure is not an energy minimum at the DFT level (see Figure 4). Although C–O bond formation between the electrophilic carbon of the R_2 ester group and the highly nucleophilic oxygen of the R_3 carboxylate substituent[31] seems chemically plausible, the ring closure obtained via GFN2-xTB optimization is clearly an artifact of the semiempirical method. M06-2X geometry optimization with the initial ring structure leads to ring opening with notable energy stabilization. Similar effect, namely, partial C–N bond formation between electrophilic carbon and nucleophilic nitrogen atoms of two different substituents is observed for the oxidized form of the **pyr-1172** molecule when optimized with the GFN2-xTB method (see Figure S6), resulting in unusually larger difference between the GFN2-xTB and M06-2X reduction potentials. Noticeable deviations from the linear fit are seen in the lower potential region as well. As exemplified by the **pyr-4528** species (see Figure 4), the GFN2-xTB method overestimates the strength of intramolecular N–H···O type hydrogen bonding interactions in these amido-pyridinium derivatives from the pyr2 molecular set, leading to lower reduction potentials as compared to full M06-2X predictions (for more details, see the Supporting Information).

The results of the benchmark studies presented in this section demonstrate that the GFN2-xTB/M06-2X method provides reasonable predictions for the redox potentials of organic molecules. The accuracy of this protocol is comparable to those of full DFT methods, but this is reached at a significantly lower computational cost. However, uncertainties arising from the semiempirical approach have been recognized for some specific

Table 1. Selection of results from the pyridinium database.[a]

NR	POT	R_3	R_1	R_2	CHG	SYS	RC
pyr-1	−1.30	COOH	P1	a1	0	pyr1	NO
pyr-2	−1.25	COOH	P1	a2	0	pyr1	NO
pyr-3	−1.35	COOH	P1	a3	0	pyr1	NO
pyr-4	−1.36	COOH	P1	a4	0	pyr1	NO
pyr-5	−1.27	COOH	P1	a5	0	pyr1	NO
pyr-6	−1.27	COOH	P1	a6	0	pyr1	NO
pyr-7	−1.34	COOH	P1	a7	0	pyr1	NO
pyr-8	−1.26	COOH	P1	a8	0	pyr1	NO
pyr-9	−1.19	COOH	P1	b1	0	pyr1	NO
pyr-10	−1.21	COOH	P1	b2	0	pyr1	NO

[a] Notation: NR - molecular label; POT-computed reduction potential (in V, referenced to SHE); R_1, R_2 and R_3-substituents as defined in Scheme 2; CHG-overall charge; SYS-molecular framework as defined in Scheme 2; RC-label for full or partial ring closure upon GFN2-xTB geometry optimization.

interactions, which was taken into account in the development of the database of pyridinium derivatives.

Analysis of reduction potentials

The GFN2-xTB/M06-2X computational protocol has been applied to the entire set of pyridinium derivatives (6712 molecules) introduced above. GFN2-xTB geometry optimizations yielded ring closure for 154 derivatives, which were identified via connectivity analysis. Additional structural inspection pointed to partial bond formation between the C atoms of electron deficient carbonyl moieties and the negatively charged groups of R_2 substituents (PO_4^{2-}, PO_3H^-, SO_3^-, CO_2^-, etc.) characterized by 1.9–2.1 Å bond distances. These cases were identified by checking the pyramidality of the carbonyl units and our test calculations revealed that these types of interactions are notably overestimated by the GFN2-xTB method (for details, see the Supporting Information). To reduce the uncertainty of the developed pyridinium database, all these molecules featuring full or partial intramolecular ring closure (altogether 328 molecules) were excluded from the analysis of reduction potentials. However, these compounds are tagged and they are included in the B6-PYR database for the sake of completeness. The computed reduction potentials for the entire set of compounds are provided in tabulated form in the Supporting Information. The first few lines of the database are shown in Table 1 for illustration. It is apparent that the reduction potential (POT) is predicted to be −1.30 V for the simplest member of the pyr1 set (R_1=R_2=CH_3, R_3=COOH), and the potential varies only slightly with the selected range of R_2 substituent. These potentials appear too low considering the limiting factor of water splitting in aqueous electrolytes,[32] so one of the most relevant questions is whether the reduction potential can be shifted to the more positive region via substituent variation.

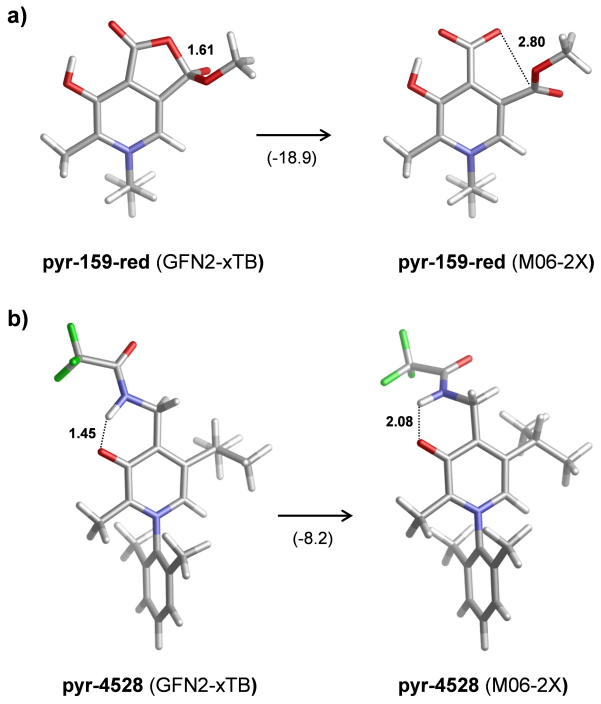

Figure 4. Differences between the optimized structures obtained with the GFN2-xTB and M06-2X methods for pyridinium derivatives a) **pyr-159-red** (reduced form of **pyr-159**) and b) **pyr-5428**. Selected bond distances are in Å. Energy changes upon M06-2X geometry optimizations from the GFN2-xTB equilibrium structures are shown in parentheses (in kcal/mol).

To assist the analysis of the present database, we developed an online tool *HistPlotly* that enables the visualization of computed data via histograms, and viewing the Lewis structures of the molecules is also possible. The computed B6-PYR database is built in *HistPlotly*, which also includes the optimized structures of the original and reduced forms of all pyridinium derivatives as well. The *HistPlotly* tool is considered as a supplementary material to the present work and it is openly available. *HistPlotly* can be applied to uploaded databases as well.[33]

The distribution of the computed standard reduction potentials is depicted in Figure 5. The predictions cover a wide potential range, between −2.9 and −0.3 V, and the region between −1.6 and −1.1 V is the most populated interval. Potentials of the pyr1 molecular set are predicted to be clearly more positive than those of the other four frameworks. This can be associated with the extended conjugated system in the pyridoxal derivatives involving the carboxyl and keto R_3 groups attached directly to the central pyridinium core, which provides

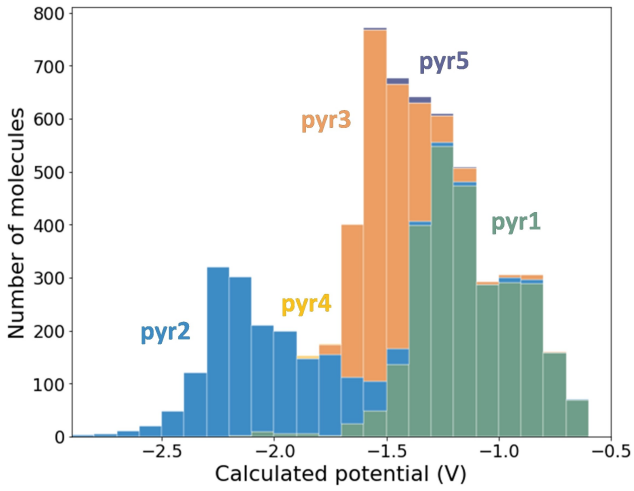

Figure 5. Distribution of calculated standard reduction potentials. The columns are colored according to the molecular subsets.

stabilization for the reduced states. Although the R_3=C(O)Ph and C(O)CF_3 groups are present in the pyridoxamine derivatives of the pyr2 set as well, direct conjugation with the pyridinium π-system is precluded. Interestingly, the potentials of pyr3 derivatives are shifted towards more positive values (with respect to their pyr2 analogues) despite their electron-donating R_3 substituents (^{i}Pr and Ph). However, we note that the pyridinium core of the pyr3 set is more electron-deficient than that of the pyr2 framework, which involves a negatively charged oxygen (deprotonated OH group). For similar reasons, the potentials of the pyr5 compounds are predicted to be more positive than those of the pyr4 set.

The effect of the nature of the R_1, R_2 and R_3 substituents on the predicted reduction potential was closely examined for the pyr1 molecular set, which is found to be the most promising framework considering that the electrochemically relevant region of the standard reduction potential is above −1.0 V.

The variation of the R_1 substituent (P1-P4 alkyl and P5-P8 aryl groups; Scheme 2) has only a minor impact on the computed potential. For a given R_2/R_3 combination, the potential changes are less than 0.2 V in the P1-P8 series, and potentials for the N-arylated species are predicted to be slightly more positive than the N-alkylated analogues.

The influence of the R_2 group is more significant; it typically varies within a 0.4 V window for a given R_1/R_3 combination. The impact of this group generally correlates with the electronic nature of the substituent. For compounds with electron donating R_2 groups (i.e. R_2=a4, f20, g8, f3, etc.; Scheme 3) computations give clearly more negative potentials than for those with electron withdrawing or cationic R_2 substituents (i.e. R_2=c5, c11, e2, e3, etc.; Scheme 3). For a few specific R_2 substituents, notably more positive potentials are predicted. Reduction potentials computed for derivatives with the *p*-nitrophenyl group (R_2=c5, Scheme 3) are exceptionally high (between −0.5 and −0.4 V) when combined with the R_3=COOH and R_3=C(O)Ph substituents. Similar potentials are predicted for molecules having the R_2=c5 substituent in the pyr2 and pyr3 sets. As demonstrated by spin density plots (Figure 6), the electron gained upon the reduction of these derivatives is delocalized over the *p*-nitrophenyl group rather than on the pyridinium core (Figure 6a). In protic solvents, the reduction of aromatic nitro compounds leads to complex irreversible reactions,[34] so these compounds are not suitable for aqueous flow battery applications.[35]

For pyridoxal derivatives with the R_2=c11 substituent (Scheme 3), computations give notably higher potentials (by about 0.4 V) as compared to those obtained for their analogues, but again only when combined with the R_3=COOH and R_3=C(O)-Ph groups. In these molecules, the spin density is also distributed mostly over the aromatic ring of the R_2 substituent (Figure 6b). For comparison, Figure 6c depicts the spin density of a radical with an electron donating R_2 substituent (R_2=g8) in

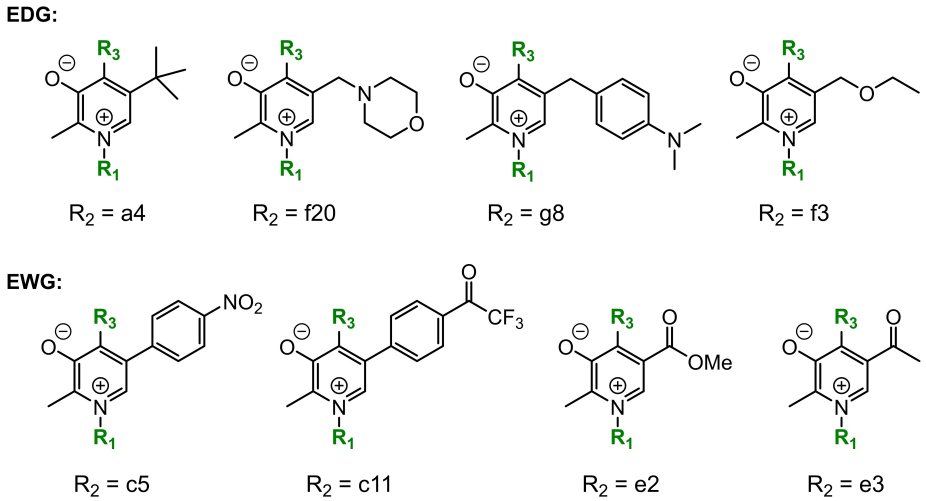

Scheme 3. Pyridoxal derivatives with electron-donating and electron withdrawing R_2 groups (EDG and EWG).

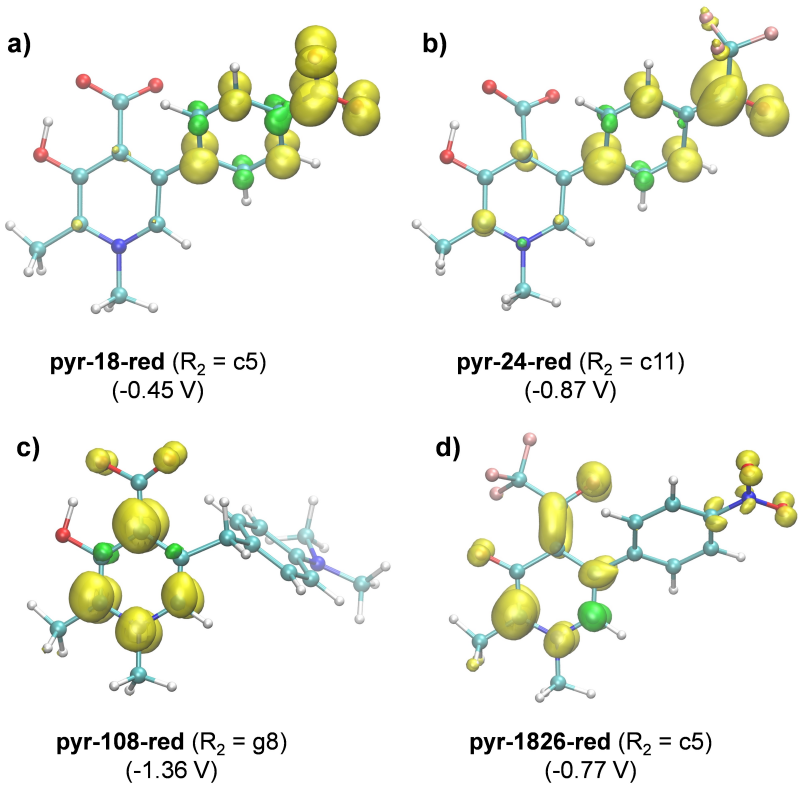

Figure 6. Spin density difference plots for selected molecules from the pyr1 set with R_1=Me: a) R_3=COOH, R_2=c5; b) R_3=COOH, R_2=c11; c) R_3=COOH, R_2=g8; d) R_3=C(O)CF_3, R_2=c5. Yellow and green colors denote an excess of α- and β-electron density (isovalue = 0.004).

this series, demonstrating that in this case the spin density is allocated to the pyridinium unit and the carboxylate group. The reduction potentials computed for molecules involving R_3=C(O)CF_3 and R_2=c5 or c11 are not exceptionally positive, because the spin density in these radicals remains on the pyridinium ring with the involvement of the carbonyl moiety of the R_3=C(O)CF_3 group (see Figure 6d). These results indicate that the central pyridinium ring may not necessarily represent the redox active unit of the molecules involved in the present molecular database, because aromatic substituents with electron withdrawing groups can favorably act as electron acceptors upon reduction (for a detailed statistical analysis of spin density distributions, see the Supporting Information).

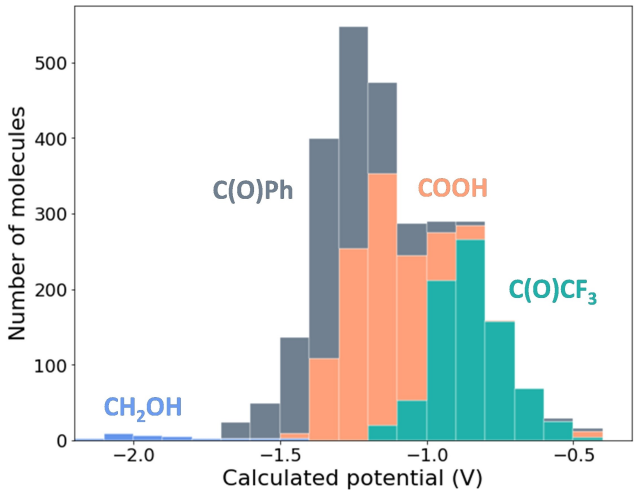

Figure 7. Distribution of calculated reduction potential for the pyr1 set as a function of R_3 substituent.

The computed potentials show the largest variation with the R_3 substituents, which is illustrated in Figure 7 for the pyr1 set. Derivatives with R_3=COOH have potentials in the region between −1.5 and −0.8 V with the maximum population at around −1.2 V. Due to the electron withdrawing effect of the R_3=C(O)CF_3 group, the potentials of these molecules are shifted towards the more positive region (above −1.0 V), whereas the potentials of molecules with the R_3=C(O)Ph group are predicted to be slightly more negative (up to −1.7 V). The reduced degree of electron delocalization in molecules with the R_3=CH_2OH substituent results in significantly lower potentials (up to −2.2 V) for these systems. The trend in the computed potential appears to be consistent with the electron donating/withdrawing properties of the four R_3 substituents, which is supported by the overall correlation between the predicted reduction potentials and the LUMO energies of the molecules (Figure 8).[36]

The analysis of molecules with potentials in the positive region above −0.8 V deserves special attention, as these compounds are expected to be within the kinetic stability window of water at pH 7. We have already noted that molecules

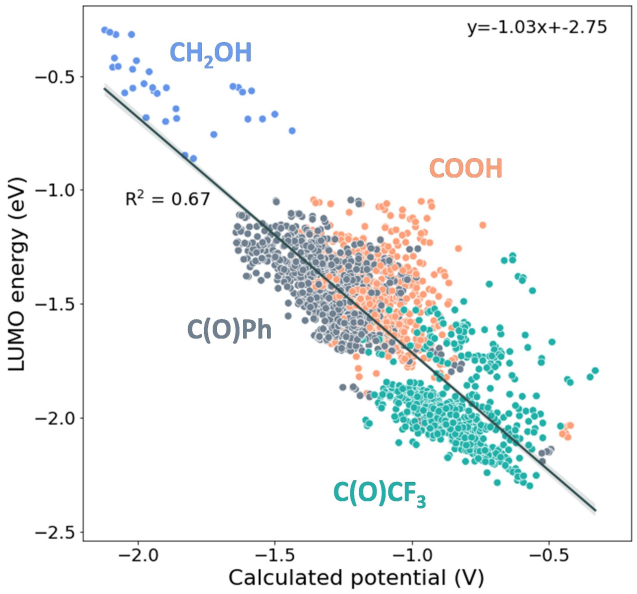

Figure 8. Correlation between potentials and lowest unoccupied molecular orbital (LUMO) energies computed for the pyr1 molecular set. Color code denotes different R_3 substituent.

belonging to the pyr1 set and having the *p*-nitrophenyl group R_2 substituent (R_2=c5) feature unusually positive potentials. Disregarding these particular cases, there are still more than 250 molecules with computed potentials above −0.8 V. All these molecules are from the pyr1 subset and have the electron withdrawing R_3=C(O)CF_3 substituent on the pyridinium framework. Interestingly, the most positive region of the computed potentials (between −0.5 and −0.3 V) is dominated by molecules involving R_2 groups that are able to form single or multiple internal H-bonds. For instance, molecules with the R_2=f27, i3 and h3 substituents (Scheme 4) involve NH groups, which enables H-bonding interaction with the oxygen of the neighbouring carbonyl group. Furthermore, the PO_3H^- and $B(OH)_2$ units of the R_2=f27 and h3 substituents allow the formation of additional internal H-bonds, as illustrated in Figure 9, which seem to affect the computed reduction potential.[37] The statistical analysis of H-bonds identified in the pyr1 database reveals that the H-bonding interactions become stronger upon the reduction processes resulting in more positive reduction potentials (for the details of the analysis, see the Supporting Information). Molecules with R_2 substituents involving cationic quaternary ammonium units (R_2=f23 and f24 in Scheme 4) tend to have higher reduction potentials as well, which is due to more favored electrostatic stabilization of the reduced states of these compounds.

Stability analysis

To assess the stability of radical species formed upon the reduction of molecules included in the present database, we applied the computational methodology suggested recently by St. John and Paton.[17,38] The basic hypothesis of this approach is that the thermodynamic stabilization of radicals is closely related to the degree of electron spin delocalization (via π-conjugation), whereas the kinetics of radical reactions can be primarily influenced by steric effects. Two computationally derived descriptors were proposed to measure these effects. The largest atomic (Mulliken) spin density (maximum spin density, s_{max}) is considered to measure the extent of spin delocalization, which defines a radical center, and the steric effect is quantified by the so-called buried volume (V_{bur}). This latter descriptor is defined as the occupied percent of the total volume of a sphere with a given radius (3.5 Å) around the radical center. This approach was validated by the authors on a dataset of ≈73 000 organic radicals. Experimentally stable radicals, such as TEMPO, for instance, was found to be characterized by low atomic spin density and high buried volume. A single stability parameter, the radical stability score

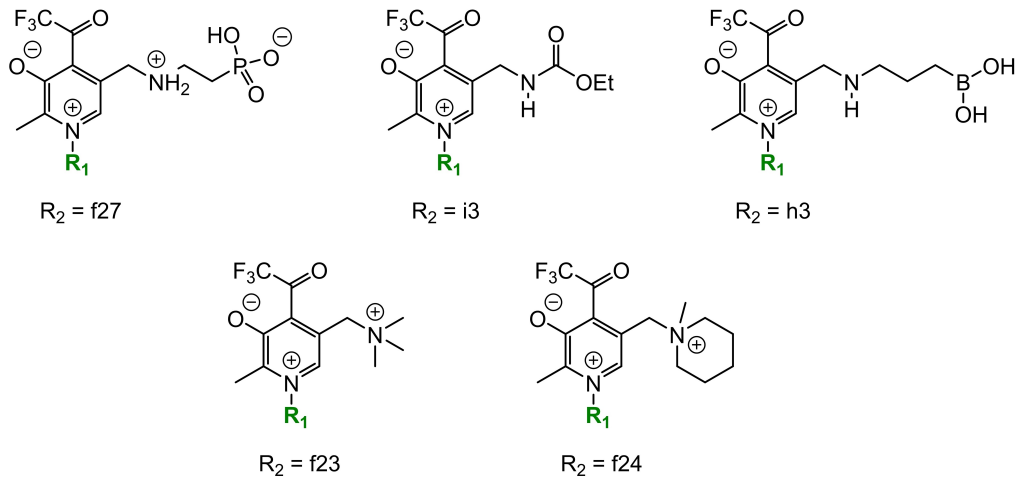

Scheme 4. Pyridoxal derivatives from the pyr1 subset with R_3=C(O)CF_3 and selected R_2 substituents. The protonation state of these molecules corresponds to pH = 7 as defined by the computational protocol.

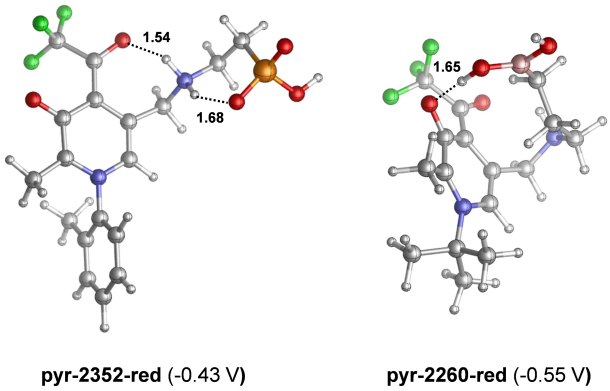

Figure 9. Illustration of H-bonding interactions in the reduced forms of **pyr-2352** and **pyr-2260** molecules. Selected bond distances are in Å. Computed reduction potentials are in V.

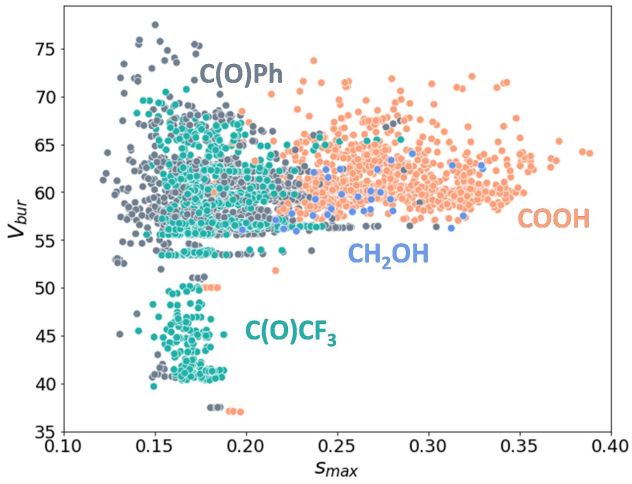

Figure 10. Computed radical stability data for the reduced forms of molecules in the pyr1 subset of the B6-PYR database. Color code denotes different R_3 substituents.

(*rss*) was also proposed, which is formulated as $rss = V_{bur} + 50 \times (1 - s_{max})$.

The distribution of stability descriptors s_{max} and V_{bur} obtained for the radical species included in the pyr1 subset of compounds is depicted in Figure 10. The computed s_{max} values are all smaller than 0.4 pointing to notable spin delocalization in these radicals. Radical species with the R_3=COOH and CH_2OH substituents are characterized by relatively large maximum spin densities (typically between 0.23 and 0.35), whereas those involving a carbonyl unit (R_3=C(O)Ph and $C(O)CF_3$) have considerably lower s_{max} values. This is in line with the more extended spin delocalization in these carbonyl compounds. The most stable radicals (lowest s_{max} and highest V_{bur}) are predicted to be from the R_3=C(O)Ph variants, but some of the radicals with R_3=$C(O)CF_3$ are predicted to have favorable stability metrics as well.

Figure 11 shows another representation of the radical stability data, namely, the stability descriptors are classified according to the atoms associated with the maximum spin densities. It is apparent that for radicals with R_3=COOH, the computational approach identifies the C6 carbon atom as the radical center. Although this atom is relatively well protected sterically by the R_3 and R_2 groups (V_{bur} is typically between 60–70), it may represent a reactive center of these radicals due to its enhanced radical character (s_{max} is typically between 0.25–

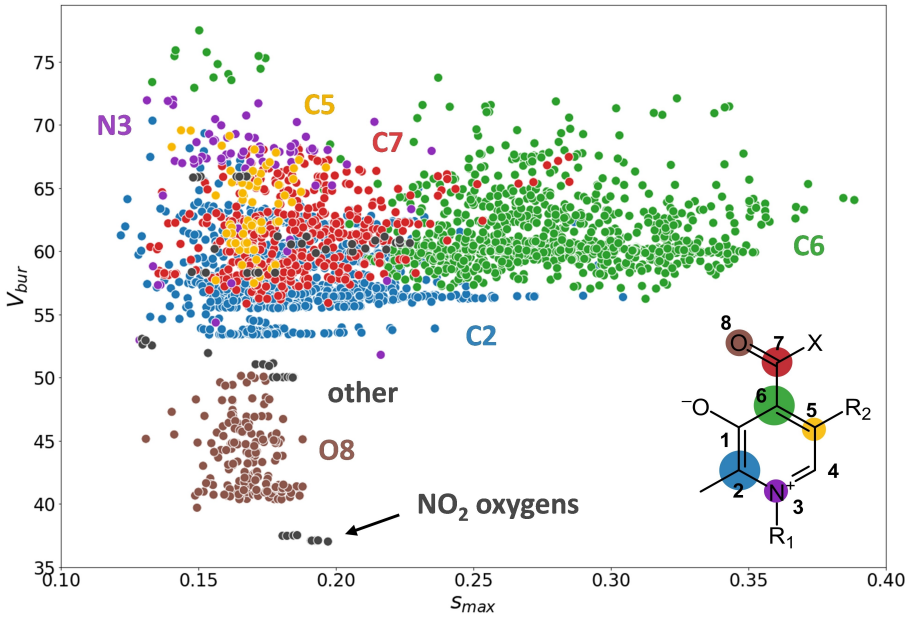

Figure 11. Computed radical stability data for the reduced forms of molecules in the pyr1 subset of the B6-PYR database. The coloring is according to the atoms of the radical centers as obtained from stability analysis. The diameter of the filled circles depicted on the keto-pyridinium framework illustrates the frequency that these atoms are classified as radical centers. Black dots denote all other radical centers (e.g. the oxygens of NO_2 substituents).

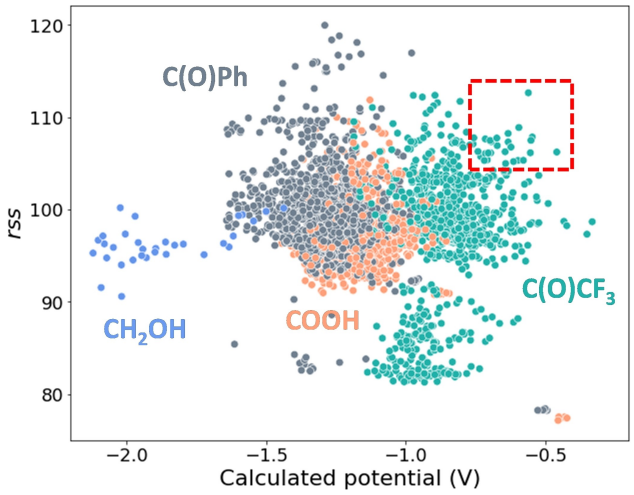

Figure 12. Computed radical stability scores as a function of calculated reduction potentials from the pyr1 molecular set. The red rectangle highlights the region of most stable radicals in the desired potential range.

0.35). In radicals with the R_3=C(O)Ph and C(O)CF_3 substituents, the C2 atom is identified as one of the most spin polarized center, but the carbonyl C7 and O8 atoms have appreciable spin densities as well. The carbonyl oxygen O8 is sterically unshielded as illustrated by the low buried volume around this radical center (between 40 and 50). The maximum spin density is associated with the pyridinium N3 atom only for a limited number of radicals, however, these nitrogen centers are protected by bulkier R_1 groups as evidenced by relatively large V_{bur} values. We also note that the radical stability analysis clearly identifies the *p*-nitrophenyl substituted compounds as unstable species in their radical forms that have unshielded NO_2 oxygen radical centers.

The computed radical stability scores (*rss*) are plotted against the calculated reduction potentials in Figure 12. The applied computational procedure suggests that there are only a few dozens of pyridoxal derivatives in the present B6-PYR database, for which our computational protocol predicts standard reduction potentials in the electrochemically favored range (above −0.8 V), and their reduced forms are classified as stable radicals according to the radical stability scores (*rss* > 105). These molecules represent the most promising candidates from the investigated B6-PYR database for experimental validation. An arbitrary selection from this set of compounds is shown in Figure 13. The 3D structure of these molecules points to increased steric bulk around the radical centers, which are typically either the C5 or the C7 carbon centers (for a complete set of molecules in this potential and *rss* range, see the Supporting Information). We note that pyridoxal derivatives with lower reduction potentials (below −0.8 V) and high radical stability scores could be of interest for the development of non-aqueous flow batteries.

The results discussed in this section demonstrate that radical stability analysis represents a promising computational tool that could be further exploited in high-throughput screening.

Summary and Conclusions

High-throughput computational screening is recognized as an efficient tool in search for new redox-active organic molecules in next-generation redox flow batteries. In our present work, we have constructed a large molecular database of *N*-functionalized pyridinium compounds derived from various B6 vitamer molecules (pyridoxal, pyridoxamine and pyridoxine), and analyzed the effect of substituent variation in these frameworks on the $1e^-$ standard reduction potential.

The computational protocol we used to predict the reduction potential of pyridinium derivatives involves several cheminformatics tools for the combinatorial generation of molecular sets from predefined pyridinium frameworks and substituents, and we apply semiempirical and DFT quantum chemical methods to compute the potentials. Benchmark calculations as referenced to experimental data demonstrate that the proposed composite GFN2-xTB/M06-2X method performs reasonably well for the prediction of redox potentials with a sufficiently low computational demand. Additional test calculations including more elaborate full DFT calculations,

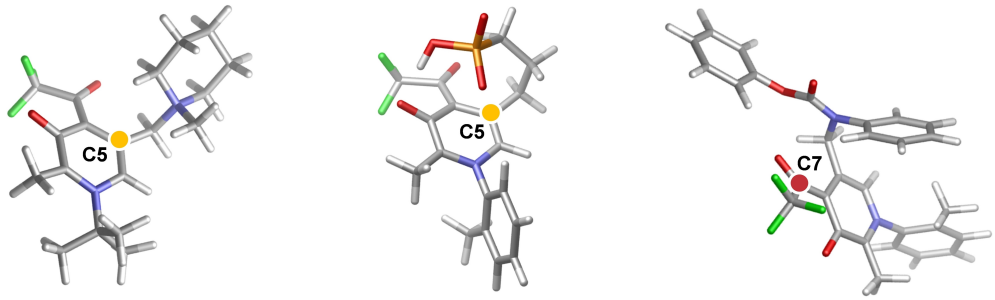

pyr-2236-red (-0.69; 107.4) **pyr-2324-red** (-0.59; 108.9) **pyr-2982-red** (-0.70; 107.5)

Figure 13. Selection of pyridoxal derivatives from the pyr1 subset of the B6-PYR database characterized by favorable reduction potential and radical stability score. Notation corresponds to the compound code used in the database. Color dots denote the radical centers obtained from stability analysis. The numbers in parenthesis are the computed potential and *rss* data.

pointed to uncertainties of the semiempirical GFN2-xTB method for some specific interactions, which had to be taken into account in our study.

The analysis of the computed reduction potentials included in the present B6-PYR database (Scheme 2) was carried out by using the *HistPlotly* online tool developed in our group. The analysis revealed that of the investigated *N*-functionalized pyridinium frameworks, only pyridoxal derivatives (molecules from the pyr1 set) give rise to relatively high standard reduction potentials compatible with the electrochemical stability of aqueous electrolytes. The carbonyl unit of the R_3 substituent in pyridoxal derivatives enables extended electron conjugation, and the potentials become sufficiently high when an electron withdrawing group (CF_3 in the present case) is attached to the carbonyl unit. The electronic effects of the R_2 substituent were found to have notable influence on the reduction potential, and the presence of internal hydrogen bonds tend to induce shift towards positive potentials. These substituent effects can be used to finetune the potentials of pyridoxal derivatives. Aromatic R_2 substituents with strong electron withdrawing groups (NO_2 or OCF_3 substituent) can act as electron acceptors by themselves, so the central pyridinium ring may not necessarily represent the redox active unit of these molecules. These electrochemical properties were clearly borne out by the present computational screening.

The stability of the reduced pyridoxal derivatives was assessed in terms of the radical stability descriptors proposed recently by St. John and Paton.[17] The radical stability analysis revealed considerable spin delocalization in radical species with R_3=C(O)Ph and $C(O)CF_3$ carbonyl substituents, but some of the atoms of the pyridoxal framework were found to have slightly enhanced radical character. Steric shielding of these centers with bulky R_2 substituents can contribute to kinetic stabilization of these radicals. Although the applied computational tool does not explicitly considers possible side reactions that are likely responsible for radical stability issues, the radical stability analysis may provide useful hints for computational screening. Based on the predicted reduction potentials and the computed radical stability scores we identified a set of N-alkylated pyridoxal derivatives in our study that could be worth considering for synthetic and electrochemical studies, which is among our future goals. Finally we note that the presented computational protocol can be readily applied to predict redox potentials for any other molecular framework. Database development for a more diverse set of molecules involved in $1e^-$ redox processes is in progress in our research group.

Acknowledgements

This project has received funding from the European Union's Horizon2020 research and innovation programme under grant agreement No 875565. Support from the Academy of Finland (projects 322899 and 348328) is also acknowledged.

Conflict of Interests

The authors declare no conflict of interest.

Data Availability Statement

The data that support the findings of this study are available in the supplementary material of this article.

Keywords: aqueous redox flow batteries · computational screening · DFT calculations · radical stability · redox potential

[1] S. Koohi-Fayegh, M. A. Rosen, *J. Energy Storage* **2020**, *27*, 101047.
[2] For challenges in large-scale electrical energy storage, see: a) B. Dunn, H. Kamath, J.-M. Tarascon, *Science* **2011**, *334*, 928–935; b) T. M. Gür, *Energy Environ. Sci.* **2018**, *11*, 2696–2767; c) A. R. Dehghani-Sanij, E. Tharumalingam, M. B. Dusseault, R. Fraser, *Renewable Sustainable Energy Revi.* **2019**, *104*, 192–208.
[3] For reviews on redox flow batteries, see: a) B. R. Chalamala, T. Soundappan, G. R. Fisher, M. R. Anstey, V. V. Viswanathan, M. L. Perry, *Proc. IEEE* **2014**, *102*, 976–999; b) F. Pan, Q. Wang, *Molecules* **2015**, *20*, 20499–20517; c) G. Zhang, L. Zhang, Y. Ding, S. Peng, X. Guo, Y. Zhao, G. He, G. Yu, *Energy Storage Mater.* **2018**, *15*, 324–350; d) Z. Li, Y. C. Lu, *Adv. Mater.* **2020**, *32*; e) E. Sánchez-Díez, E. Ventosa, M. Guarnieri, A. Trovò, C. Flox, R. Marcilla, F. Soavi, P. Mazur, E. Aranzabe, R. Ferret, *J. Power Sources* **2021**, *481*, 228804; f) M. L. Perry, K. E. Rodby, F. R. Brushett, *ACS Energy Lett.* **2022**, *7*, 659–667.
[4] For reviews on vanadium-based redox flow batteries, see: a) G. Kear, A. A. Shah, F. C. Walsh, *Int. J. Energy Res.* **2012**, *36*, 1105–1120; b) A. H. Whitehead, T. J. Rabbow, M. Trampert, P. Pokorny, *J. Power Sources* **2017**, *351*, 1–7
[5] For reviews on organic FBs, see: a) W. Wang, V. Sprenkle, *Nat. Chem.* **2016**, *8*, 204–206; b) J. Winsberg, T. Hagemann, T. Janoschka, M. D. Hager, U. S. Schubert, *Angew. Chem. Int. Ed.* **2017**, *56*, 686–711; c) P. Leung, A. A. Shah, L. Sanz, C. Flox, J. R. Morante, Q. Xu, M. R. Mohamed, C. Ponce de León, F. C. Walsh, *J. Power Sources* **2017**, *360*, 243–283; d) C. Zhang, L. Zhang, Y. Ding, S. Peng, X. Guo, Y. Zhao, G. He, G. Yu, *Energy Storage Mater.* **2018**, *15*, 324–350; e) Y. Ding, C. Zhang, L. Zhang, Y. Zhou, G. Yu, *Chem. Soc. Rev.* **2018**, *47*, 69–103; f) R. Chen, *ChemElectroChem* **2019**, *6*, 603–612; g) J. Cao, J. Tian, J. Xu, Y. Wang, *Energy Fuels* **2020**, *34*, 13384–13411; h) X. Fang, Z. Li, Y. Zhao, D. Yue, L. Zhang, X. Wei, *ACS Mater. Lett.* **2022**, *4*, 277–306.
[6] For reviews on aqueous organic FBs, see: a) S. Gentil, D. Reynard, H. H. Girault, *Curr. Opin. Electrochem.* **2020**, *21*, 7–13; b) J. Cao, J. Tian, J. Xu, Y. Wang, *Energy Fuels* **2020**, *34*, 13384–13411; c) D. G. Kwabi, Y. Ji, M. J. Aziz, *Chem. Rev.* **2020**, *120*, 6467–6489; d) P. Fischer, P. Mazúr, J. Krakowiak, *Molecules* **2022**, *27*, 560; e) Q. Chen, Y. Lv, Z. Yuan, X. Li, G. Yu, Z. Yang, T. Xu, *Adv. Funct. Mater.* **2022**, *32*, 2108777.
[7] For a review on non-aqueous organic FBs, see: M. Li, Z. Rhodes, J. R. Cabrera-Pardo, S. D. Minteer, *Sustain. Energy Fuels* **2020**, *4*, 4370–4389.
[8] For a recent review on molecular modeling of organic redox-active battery materials, see: R. P. Fornari, P. Silva, *WIREs Comput. Mol. Sci.* **2021**, *11*, e1495.
[9] a) M. T. Huynh, C. W. Anson, A. C. Cavell, S. S. Stahl, S. Hammes-Schiffer, *J. Am. Chem. Soc.* **2016**, *138*, 15903–15910; b) Y. K. Han, C. S. Jin, *Curr. Appl. Phys.* **2018**, *18*, 1507–1512; c) R. P. Fornari, M. Mesta, J. Hjelm, T. Vegge, P. D. Silva, *ACS Mater. Lett.* **2020**, *2*, 239–246; d) S. Schwan, D. Schröder, H. A. Wegner, J. Janek, D. Mollenhauer, *ChemSusChem* **2020**, *13*, 5480–5488.
[10] a) C. de la Cruz, A. Molina, N. Patil, E. Ventosa, R. Marcilla, A. Mavrondakis, *Sustain. Energy Fuels* **2020**, *4*, 5513–5521; b) Q. Zhang, A. Khetan, E. Sorkun, S. Er, *J. Mater. Chem. A* **2022**, *10*, 22214–22227.
[11] For basic concepts of high-throughput computational screening in FB research, see: a) J. Hachmann, R. Olivares-Amaya, S. Atahan-Evrenk, C. Amador-Bedolla, R. S. Sánchez-Carrera, A. Gold-Parker, L. Vogt, A. M. Brockway, A. Aspuru-Guzik, *J. Phys. Chem. Lett.* **2011**, *2*, 2241–2251; b) E. O. Pyzer-Knapp, C. Suh, R. Gómez-Bombarelli, J. Aguilera-Iparraguirre, A. Aspuru-Guzik, *Annu. Rev. Mater. Res.* **2015**, *45*, 195–216; c) L.

Cheng, R. S. Assary, X. Qu, A. Jain, S. P. Ong, N. N. Rajput, K. Persson, L. A. Curtiss, *J. Phys. Chem. Lett.* **2015**, *6*, 283–291.
[12] a) S. Er, C. Suh, M. P. Marshak, A. Aspuru-Guzik, *Chem. Sci.* **2015**, *6*, 885–893; b) S. D. P. Flores, G. C. Martin-Noble, R. L. Phillips, J. Schrier, *J. Phys. Chem. C* **2015**, *119*, 21800–21809; c) K. M. Pelzer, L. Cheng, L. A. Curtiss, *J. Phys. Chem. C* **2017**, *121*, 237–245; d) D. P. Tabor, R. Gómez-Bombarelli, L. Tong, R. G. Gordon, M. J. Aziz, A. Aspuru-Guzik, *J. Mater. Chem. A* **2019**, *7*, 12833–12841; e) S. B. Kristensen, T. van Mourik, T. B. Pedersen, J. L. Sørensen, J. Muff, *Sci. Rep.* **2020**, *10*, 13571; f) Q. Zhang, A. Khetan, E. Sorkun, F. Niu, A. Loss, I. Pucher, S. Er, *Energy Storage Mater.* **2022**, *47*, 167–177; g) A. Khetan, *Batteries* **2023**, *9*, 24–27.
[13] a) F. A. Faber, L. Hutchison, B. Huang, J. Gilmer, S. S. Schoenholz, G. E. Dahl, O. Vinyals, S. Kearnes, P. F. Riley, O. A. V. Lilienfeld, *J. Chem. Theory Comput.* **2017**, *13*, 5255–5264; b) A. Jinich, B. Sanchez-Lengeling, H. Ren, R. Harman, A. Aspuru-Guzik, *ACS Cent. Sci.* **2019**, *5*, 1199–1210; c) J. P. Janet, S. Ramesh, C. Duan, H. J. Kulik, *ACS Cent. Sci.* **2020**, *6*, 513–524; d) J. Barker, L. S. Berg, J. Hamaekers, A. Maass, *Batteries & Supercaps* **2021**, *4*, 1482–1490; e) G. Agarwal, H. A. Doan, L. A. Robertson, L. Zhang, R. S. Assary, *Chem. Mater.* **2021**, *33*, 8133–8144; f) S. Ghule, S. R. Dash, S. Bagchi, K. Joshi, K. Vanka, *ACS Omega* **2022**, *7*, 11742–11755.
[14] For recent contributions on viologen derivatives, see: a) L. Striepe, T. Baumgartner, *Chem. Eur. J.* **2017**, *23*, 16924–16940; b) J. Huang, Z. Yang, V. Murugesan, E. Walter, A. Hollas, B. Pan, R. S. Assary, I. A. Shkrob, X. Wei, Z. Zhang, *ACS Energy Lett.* **2018**, *3*, 2533–2538; c) S. Hu, T. Li, M. Huang, J. Huang, W. Li, L. Wang, Z. Chen, Z. Fu, X. Li, Z. Liang, *Adv. Mater.* **2021**, *33*, 2005839; d) Z. Burešová, M. Klikar, P. Mazúr, M. Mikešová, J. Kvíčala, T. Bystron, F. Bureš, *Front. Chem.* **2021**, *8*, 631477; e) K. Rak, M. Klikar, Z. Burešová, P. Mazúr, M. Mikešová, J. Kvíčala, F. Bureš, *Org. Biomol. Chem.* **2021**, *19*, 8830–8839; f) G. Tang, Y. Liu, Y. Li, K. Peng, P. Zuo, Z. Yang, T. Xu, *J. Am. Chem. Soc.* **2022**, *2*, 1214–1222; g) X. Liu, X. Zhang, G. Li, S. Zhang, B. Zhang, W. Ma, Z. Wang, Y. Zhang, G. He, *J. Mater. Chem. A* **2022**, *10*, 9830–9836.
[15] a) C. S. Sevov, R. E. M. Brooner, E. Chénard, R. S. Assary, J. S. Moore, J. Rodríguez-López, M. S. Sanford, *J. Am. Chem. Soc.* **2015**, *137*, 14465–14472; b) C. S. Sevov, K. H. Hendriks, M. S. Sanford, *J. Phys. Chem. C* **2017**, *121*, 24376–24380; c) K. H. Hendriks, C. S. Sevov, M. E. Cook, M. S. Sanford, *ACS Energy Lett.* **2017**, *2*, 2430–2435; d) C. S. Sevov, D. P. Hickey, M. E. Cook, S. G. Robinson, S. Barnett, S. D. Minteer, M. S. Sigman, M. S. Sanford, *J. Am. Chem. Soc.* **2017**, *139*, 2924–2927.
[16] a) J. S. Casas, A. Castiñeiras, F. Condori, M. D. Couce, U. Russo, A. Sánchez, J. Sordo, J. M. Varela, *Eur. J. Inorg. Chem.* **2003**, *15*, 2790–2797; b) K. L. Ericson, V. M. Maloney, J. D. Mahuren, S. P. Coburn, T. P. Degenhardt, *Bioorg. Med. Chem. Lett.* **2008**, *18*, 1845–1848.
[17] S. V. S. Sowndarya, P. C. St. John, R. S. Paton, *Chem. Sci.* **2021**, *12*, 13158–13166.
[18] For methodological developments, benchmark studies, and suggested protocols regarding the calculation of redox potential, see: a) M. Isegawa, F. Neese, D. A. Pantazis, *J. Chem. Theory Comput.* **2016**, *12*, 2272–2284; b) P. M. Tagade, S. P. Adiga, M. S. Park, S. Pandian, K. S. Hariharan, S. M. Kolake, *J. Phys. Chem. C* **2018**, *122*, 11322–11333; c) C. M. Sterling, R. Bjornsson, *J. Chem. Theory Comput.* **2019**, *15*, 52–67; d) Q. Zhang, A. Khetan, S. Er, *Sci. Rep.* **2020**, *10*, 22149; e) H. Neugebauer, F. Bohle, M. Bursch, A. Hansen, S. Grimme, *J. Phys. Chem. A* **2020**, *124*, 7166–7176; f) A. R. McNeill, S. E. Bodman, A. M. Burney, C. D. Hughes, D. L. Crittenden, *J. Phys. Chem. C* **2020**, *124*, 24105–24114; g) E. Hruska, A. Gale, F. Liu, *J. Chem. Theory Comput.* **2022**, *18*, 1096–1108; h) L. Tomaník, L. Rulíšek, P. Slavíček, *J. Chem. Theory Comput.* **2023**, *19*, 1014–1022.
[19] For computational approaches to molecular solubilities, see: a) J. J. Guerard, J. S. Arey, *J. Chem. Theory Comput.* **2013**, *9*, 5046–5058; b) J. L. McDonagh, N. Nath, L. D. Ferrari, T. V. Mourik, J. B. O. Mitchell, *J. Chem. Inf. Model.* **2014**, *54*, 844–856; c) S. Kim, A. Jinich, A. Aspuru-Guzik, *J. Chem. Inf. Model.* **2017**, *57*, 657–668; d) L. Ward, N. Dandu, B. Blaiszik, B. Narayanan, R. S. Assary, P. C. Redfern, I. Foster, L. A. Curtiss, *J. Phys. Chem. A* **2021**, *125*, 5990–5998.
[20] For computational studies on stabilities, see: a) Refs. [12b] and [17]; b) R. S. Assary, L. Zhang, J. Huang, L. A. Curtiss, *J. Phys. Chem. C* **2016**, *120*, 14531–14538.
[21] Schrödinger Release 2017–1: CombiGlide and LigPrep, Schrödinger, LLC, New York, NY, **2017**
[22] a) N. M. O'Boyle, M. Banck, C. A. James, C. Morley, T. Vandermeersch, G. R. Hutchison, *J. Cheminf.* **2011**, *3*, 33; b) Open Babel: The Open Source Chemistry Toolbox, http://openbabel.org.
[23] a) S. Grimme, C. Bannwarth, P. Shushkov, *J. Chem. Theory Comput.* **2017**, *13*, 1989–2009; b) C. Bannwarth, S. Ehlert, S. Grimme, *J. Chem. Theory Comput.* **2019**, *15*, 1652–1671.
[24] User Guide to Semiempirical Tight Binding, https://xtb-docs.readthedocs.io/en/latest/contents.html.
[25] P. Pracht, F. Bohle, S. Grimme, *Phys. Chem. Chem. Phys.* **2020**, *22*, 7169–7192.
[26] Y. Zhao, D. G. Truhlar, *Theor. Chem. Acc.* **2008**, *120*, 215–241.
[27] M. J. Frisch, G. W. Trucks, H. B. Schlegel, G. E. Scuseria, M. A. Robb, J. R. Cheeseman, G. Scalmani, V. Barone, G. A. Petersson, H. Nakatsuji, X. Li, M. Caricato, A. V. Marenich, J. Bloino, B. G. Janesko, R. Gomperts, B. Mennucci, H. P. Hratchian, J. V. Ortiz, A. F. Izmaylov, J. L. Sonnenberg, D. Williams-Young, F. Ding, F. Lipparini, F. Egidi, J. Goings, B. Peng, A. Petrone, T. Henderson, D. Ranasinghe, V. G. Zakrzewski, J. Gao, N. Rega, G. Zheng, W. Liang, M. Hada, M. Ehara, K. Toyota, R. Fukuda, J. Hasegawa, M. Ishida, T. Nakajima, Y. Honda, O. Kitao, H. Nakai, T. Vreven, K. Throssell, J. A. Montgomery Jr., J. E. Peralta, F. Ogliaro, M. J. Bearpark, J. J. Heyd, E. N. Brothers, K. N. Kudin, V. N. Staroverov, T. A. Keith, R. Kobayashi, J. Normand, K. Raghavachari, A. P. Rendell, J. C. Burant, S. S. Iyengar, J. Tomasi, M. Cossi, J. M. Millam, M. Klene, C. Adamo, R. Cammi, J. W. Ochterski, R. L. Martin, K. Morokuma, O. Farkas, J. B. Foresman, D. J. Fox, Gaussian 16, Revision C.01, *Gaussian, Inc.*, Wallingford CT **2016**.
[28] A. V. Marenich, C. J. Cramer, D. G. Truhlar, *J. Phys. Chem. B* **2009**, *113*, 6378–6396.
[29] A. A. Isse, A. Gennaro, *J. Phys. Chem. B* **2010**, *114*, 7894–7899.
[30] H. G. Roth, N. A. Romero, D. A. Nicewicz, *Synlett* **2016**, *27*, 714–723.
[31] We note that computations predict that the R_3═COOH group of the pyr1 molecular set is always deprotonated by the negatively charged oxygen of the pyridoxal framework, so the oxygen of this R_3 group becomes highly nucleophilic.
[32] F. Wan, J. Zhu, S. Huang, Z. Niu, *Batteries & Supercaps* **2020**, *3*, 323–330.
[33] *HistPlotly* is available at https://histplotly.ttk.hu/. Further details are provided in the Supporting Information.
[34] For a recent review, see: T. Wirtanen, E. Rodrigo, S. R. Waldvogel, *Adv. Synth. Catal.* **2020**, *362*, 2088–2101.
[35] For a potential application of nitrobenzene in nonaqueous organic flow batteries, see: B. Liu, C. W. Tang, C. Zhang, G. Jia, T. Zhao, *Chem. Mater.* **2021**, *33*, 978–986.
[36] For contributions discussing the correlation between reduction potentials and LUMO energies, see: a) Refs. [10b] and [18b]; b) R. S. Assary, F. R. Brushett, L. A. Curtiss, *RSC Adv.* **2014**, *4*, 57442–57451.
[37] For contributions discussing the effect of H-bonding interactions on the redox potentials, see: Refs. [9a], [9c] and [9d].
[38] For alternative descriptors of radical stabilities, see: a) M. L. Coote, C. Y. Lin, A. L. J. Beckwith, A. A. Zavitsas, *Phys. Chem. Chem. Phys.* **2010**, *12*, 9597–9610; b) J. Hioe, H. Zipse, *Org. Biomol. Chem.* **2010**, *8*, 3609–3617.

Manuscript received: March 30, 2023
Accepted manuscript online: May 19, 2023
Version of record online: June 30, 2023